ACS NANO

www.acsnano.org

Diffusion Channel Engineering of Spinel Cathodes for Selective Lithium Extraction from Low-Grade Brine

Yixuan Qiao, Houjun Zhang, Yao Nian, Yuqi Li, Changwei Xiao, Tiantian Wang, Yang Wang,* Mingjian Wen, You Han, and Jieshan Qiu*

Cite This: https://doi.org/10.1021/acsnano.5c14948 Read Online

ACCESS | Metrics & More | Article Recommendations | Supporting Information

ABSTRACT: The surging demand for lithium to power electric vehicles and grid-scale energy storage highlights the urgent need for sustainable extraction from unconventional resources, such as low-grade salt lake brines. Electrochemical lithium extraction offers an energy-efficient pathway, yet its progress is constrained by the limited selectivity and poor durability of the cathode material, such as $LiMn_2O_4$ (LMO). Here, we demonstrate that Nb doping effectively tunes the three-dimensional Li^+ diffusion channels of LMO, simultaneously lowering the Mn valence, enlarging the lattice constant, and strengthening the Mn−O framework. The structural optimization delivers a discharge capacity of 107 mAh g^{-1} and markedly reduces the Li^+ diffusion resistance, thereby lowering the energy consumption of lithium extraction (4.83 Wh mol^{-1}). In highly complex Qarhan brine with an extremely high ratio of competing ions, Nb-doped LMO exhibits considerable Li^+ extraction capacity (5.21 mmol g^{-1} in Qarhan raw brine and 3.79 mmol g^{-1} in Qarhan old brine), superior Li^+ selectivity (Li^+/Mg^{2+} = 48.47 and Li^+/Na^+ = 44.42), and enhanced cyclic stability (Li^+ intercalation capacity retention 72.09% after 50 cycles). Depth-resolved TOF-SIMS and DFT analyses reveal that the broadened diffusion channels suppress bulk diffusion of Na^+ and Mg^{2+} while reducing the Li^+ migration barrier, underpinning the high selectivity. These results suggest that Nb-doped LMO is a robust and scalable cathode for electrochemical lithium extraction, offering a viable strategy to unlock lithium from low-grade brines.

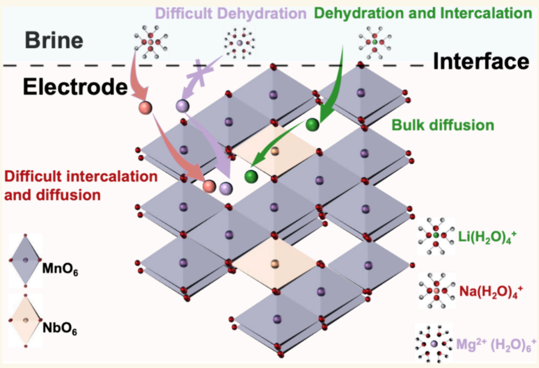

KEYWORDS: *electrochemical lithium extraction, low-grade brine, diffusion channel engineering, high-valent doping, lithium selectivity*

INTRODUCTION

Lithium-ion batteries (LIBs) of high energy density play a critical role in enabling clean energy transition and advancing a low-carbon society.[1] The accelerating deployment of electric vehicles and grid-scale energy storage has created an unprecedented demand for lithium resources,[2−4] a trend projected to continue growing over the next 20 years.[5] Conventional lithium sources, primarily high-grade lithium ores,[6,7] are geographically concentrated and expected to be depleted by 2080.[8] In contrast, salt lake brines—containing abundant and underutilized lithium resources—have emerged as a sustainable alternative for lithium extraction.[9] However, brines contain significantly high concentrations of competing cations (Na^+, Mg^{2+}, K^+, Ca^{2+}),[10] posing an exceptional challenge for selective lithium extraction.[11]

Traditional lithium extraction techniques from low-quality brines, such as solar evaporation, have several limitations, including their time-consuming nature and vulnerability to environmental factors.[12] Direct lithium extraction (DLE) technologies have emerged as promising approaches, offering higher lithium extraction efficiency.[13] DLE technologies, such as membrane-based separation,[14] lithium-ion sieve,[15,16] and solvent extraction,[17] face challenges like membrane fouling and consumption of chemicals.[18,19] Electrochemical lithium extraction is particularly attractive owing to the high selectivity,[20] chemical-free regeneration, and rapid extraction rate.[21,22] Electrochemical lithium extraction is driven by an electric field, where Li^+ from brine is selectively captured, while Cl^- (or other anions) can be adsorbed by the anode. By reversing the

Received: September 1, 2025
Revised: November 25, 2025
Accepted: November 25, 2025

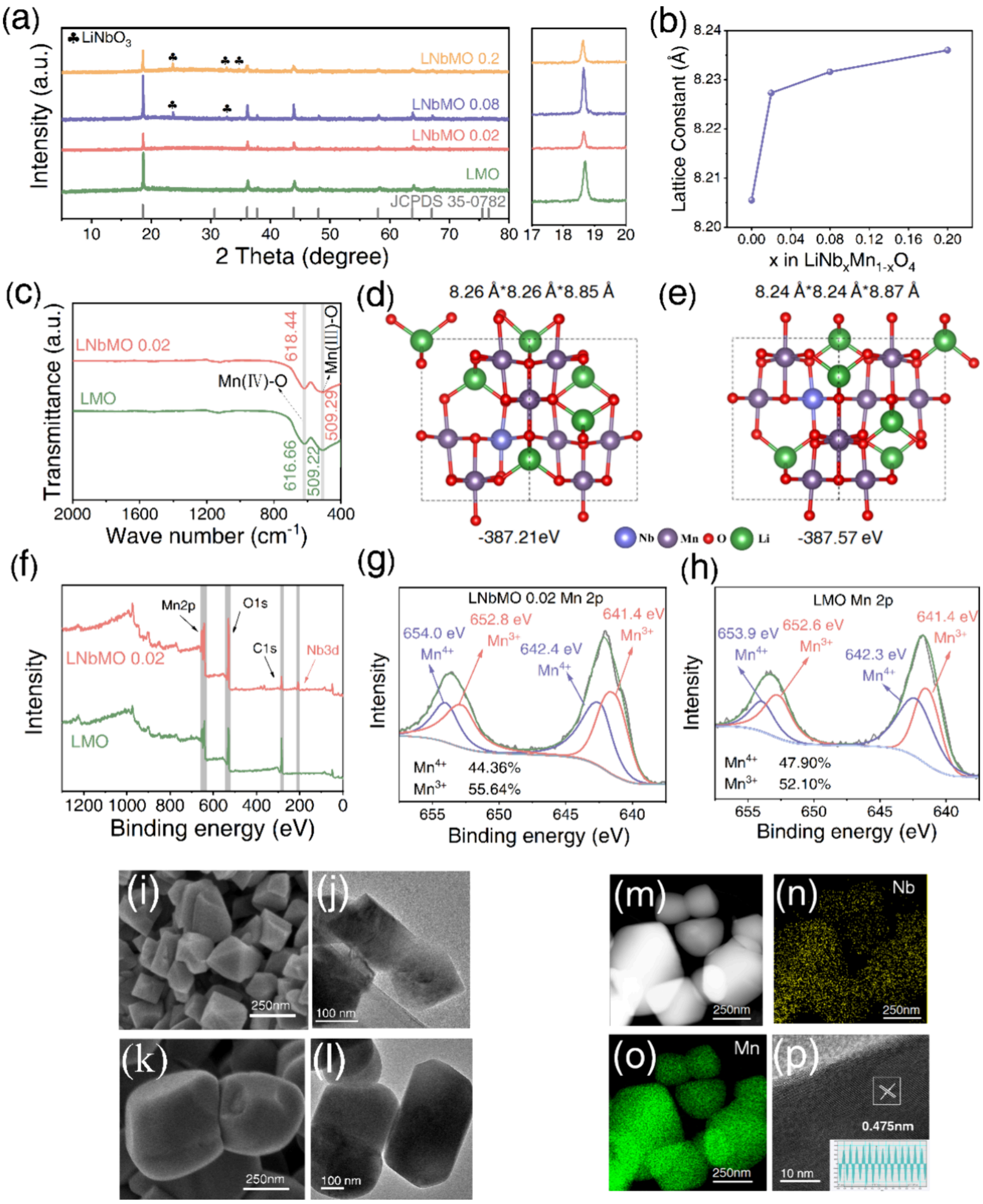

Figure 1. (a) XRD patterns showing the (111) lattice plane of LMO with different Nb doping amounts. (b) Lattice constant of LMO with different Nb doping amounts. (c) FT-IR spectra of LMO and LNbMO 0.02. Structural energy of LNbMO with Nb doping at (d) Mn^{3+} and (e) Mn^{4+} sites. (f) XPS survey spectra for LMO and LNbMO 0.02. (g, h) High-resolution XPS spectra of Mn 2p of (g) LNbMO 0.02 and (h) LMO. (i) FESEM images of LMO. (j) TEM image of LMO. (k) FESEM images of LNbMO 0.02. (l) TEM image of LNbMO 0.02. (m−o) HAADF-STEM images and elemental mapping images of LNbMO 0.02. (p) HRTEM image displaying the (111) lattice plane of LNbMO 0.02.

current, Li^+ and Cl^- can be released into the receiving solution, realizing LiCl enrichment.[23,24]

The performance of electrochemical lithium extraction is dictated by the cathode material, which exploits the distinct radii, lattice energies, and hydration energies of Li^+ and competing cations to achieve selective capture.[25] Spinel LMO has received widespread attention due to its unique lattice structure, the abundance of Mn, and low cost.[26,27] The three-dimensional diffusion channel and unique Li^+ tetrahedral coordination sites in the crystal structure provide LMO with an impressive theoretical intercalation capacity of 5.75 mmol g^{-1} and remarkable selectivity for Li^+ over a wide range of coexisting competing cations.[28] However, the Jahn−Teller effect and disproportionation reaction of Mn^{3+} result in structural distortion and Mn dissolution, which can lead to capacity degradation[29,30] and thus severely hinder its practical deployment.

A promising route to overcome these limitations lies in lattice and channel engineering through heteroatom doping.[31−33] From the perspective of increasing the average valence of Mn to alleviate Mn dissolution, lower-valence elements (less than or equal to +3) such as Li^+,[23] Ni^{2+},[34] Co^{2+},[35] Cr^{3+},[36] and Al^{3+}[37] are typically selected as dopants to substitute Mn^{3+}. Theoretically, these dopants have difficulties in providing high capacity due to the reduced Mn^{4+}/Mn^{3+} cation-redox capacity.[38,39] Moreover, boosting the bond energy

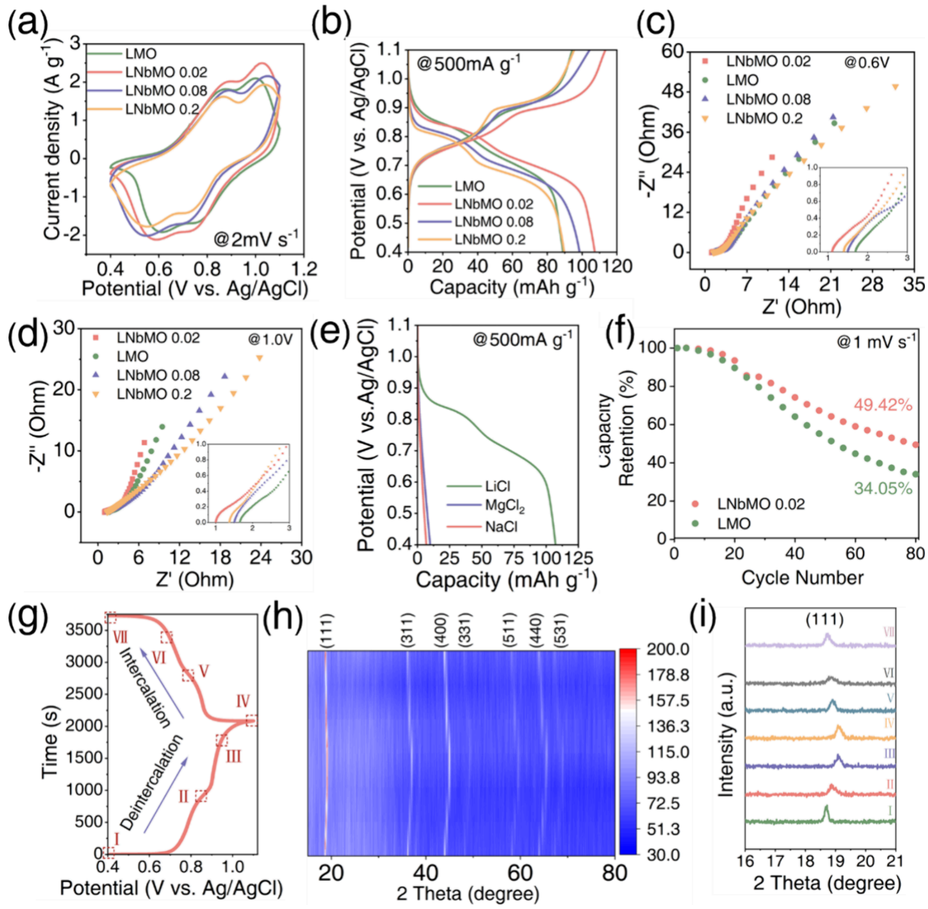

Figure 2. (a) CV curves of LMO with different Nb doping amounts at a scan rate of 2 mV s^{-1} in 0.5 M LiCl solution. (b) Charge and discharge curves of LMO with different Nb doping amounts under an applied current of 500 mA g^{-1} in 0.5 M LiCl solution. (c) EIS curves of all samples under 0.6 V (vs Ag/AgCl). (d) EIS curves of all samples under 1.0 V (vs Ag/AgCl). (e) Discharge curves of LNbMO 0.02 in 0.5 M LiCl, $MgCl_2$, and NaCl solutions. (f) Capacitance retentions of LMO and LNbMO 0.02 after 80 CV cycles at a scan rate of 1 mV s^{-1} in 0.5 M LiCl solution. (g) Charge and discharge curve under 250 mA g^{-1} in 0.5 M LiCl solution corresponding to the ex situ XRD. (h) Contour map showing the shift of crystal planes for LNbMO 0.02 during the charge−discharge period. (i) Ex situ XRD patterns showing the shift of the (111) lattice plane LNbMO 0.02 during the charge−discharge period.

is also a solution, and high-valence elements can generally provide higher bond energy than Mn−O. For example, the bond energy of Ti−O is higher than that of Mn−O,[40] which stabilizes the spinel framework of LMO and reduces Mn dissolution. Thus, high-valence elements as dopants have the capability of stabilizing the spinel framework without sacrificing the redox activity. To date, the specific mechanisms of high-valent dopants (such as Nb^{5+}, V^{5+}) for electrochemical lithium extraction remain unclear and require further investigation.

In this work, we report a high-valent Nb-doping strategy that broadens the Li^+ diffusion channel of LMO, lowers the Mn valence, and strengthens the Mn−O framework. These modifications yield a high capacity, reduced Li^+ diffusion resistance, and enhanced cyclic stability. The electrochemical lithium extraction performance in low-grade Qarhan brine (rather than simulated brines[41]) shows an improved Li^+ selectivity and increased extraction capacity. TOF-SIMS and density functional theory (DFT) analyses reveal that channel engineering suppresses bulk diffusion of competing ions while lowering the Li^+ migration barrier, providing a mechanistic basis for selective lithium transport. More importantly, this work introduces diffusion channel engineering via high-valent doping as a generalizable design principle for advancing electrochemical separation technologies.

RESULTS AND DISCUSSION

The broadened Li^+ transport channel via Nb doping is first confirmed by XRD and DFT. The main diffraction peaks of all samples are indexed to spinel-type $LiMn_2O_4$ (JCPDS 35-0782) in Figure 1a, suggesting no influence of surface Nb doping on the spinel crystal structure. The (111) lattice plane of Nb-doped LMO shows a slight shift to a lower 2θ degree with increasing Nb doping amount, corresponding to the enlarged lattice constant according to the results in Figure 1b calculated by the least-squares method. This suggests that Nb^{5+} can have a significant effect on the lattice constant of LMO even with a low doping amount. In addition, the impurity phase of $LiNbO_3$ can be detected with increased Nb doping amount, which may affect the electrochemical properties,[42] and the intensity of the impurity phase is more obvious in LNbMO 0.2. Functional groups in LMO and LNbMO 0.02 are detected through FT-IR spectra, as shown in Figure 1c, where both samples display two principal vibration bands attributed to the Mn(III)-O and Mn(IV)-O of MnO_6 octahedron.[43,44] The vibration band of Mn(IV)-O at around 616.66 cm^{-1} exhibits a slight blue shift to 681.44 cm^{-1} after Nb doping, confirming a higher bond energy

https://doi.org/10.1021/acsnano.5c14948

of Nb−O than that of Mn−O, which is beneficial for a greater structural stability. Additionally, no obvious shift occurs on the vibration band of Mn(III)-O after Nb doping, meaning that Nb mainly substitutes for Mn^{4+} in the spinel structure. To further analyze the substitution site (Mn (III) or Mn (IV)) of Nb, the structural energy of different LNbMO structures is calculated in Figure 1d,e (The original structure of LMO is exhibited in Figures S1and S2). When Nb is doped at the Mn (IV) site, the structural energy of LNbMO reaches −387.57 eV, which is lower than that of Nb doping at the Mn (III) site (−387.21 eV), indicating that Nb prefers to dope at the Mn (IV) site, facilitating a more stable crystal structure. In Figures 1f and S3, compared to LMO, an obvious Nb 3d peak at 205−210 eV can be observed in the XPS spectra of LNbMO 0.02, confirming the successful surface Nb doping by the solid-state reaction. As shown in Figures 1 g,h and S4, after Nb doping, the peak fitting for Mn 2p results shows that the atomic content of Mn^{4+} in LNbMO 0.02 slightly decreases from 47.90 to 44.36%, while that of Mn^{3+} increases from 52.10 to 55.64%, proving the substitution of Nb for Mn^{4+}. Therefore, Nb doping reduces the average valence state of Mn, leading to a higher capacity from more redox reactions of $Mn^{3+/4+}$. Additionally, in Figure S5, the percentage of O_{lat} (metal−O bonds) increased while the O_{def} (defects of oxygen) fraction slightly decreased, accompanied by a slight positive shift (≈+ 0.05 eV) of the O_{lat} binding energy. These changes indicated fewer oxygen-vacancy and -defect states and a stronger metal−oxygen framework, which means a more stable structure and capacity retention. Predelithiation is an important procedure for the materials to be applied in electrochemical lithium extraction. After the electrochemical delithiation process (Figure S6), the (111) crystal plane of LNbMO 0.02 demonstrates a slight shift to a higher 2θ degree in Figure S7, indicating the lattice shrinkage and creating sufficient lithium vacancies in the spinel structure of LNbMO 0.02.

The morphologies of LMO and LNbMO 0.02 obtained from FESEM exhibit a typical octahedral appearance in Figure 1i−l. After Nb doping, the particle size significantly increases, while the morphology transforms to truncated octahedral. This effectively reduces the area of the (111) lattice plane, which brings the possibility to alleviate Mn dissolution.[45] In Figure S8, the average particle size was significantly enlarged after Nb doping, from 170.61 ± 51.78 to 419.45 ± 112.28 nm. Similarly, TEM images show an enlarged particle size and truncated octahedral morphology after Nb doping. The elemental mapping of LNbMO 0.02 confirms the successful doping from the uniform Nb distribution in Figures 1 m−o and S9. Furthermore, the HRTEM images in Figure 1 p demonstrate the lattice fringes with a spacing of 0.475 nm, corresponding to the (111) crystal plane of LNbMO of 0.02, which is consistent with the XRD patterns. Moreover, the specific surface area and pore distribution of LMO and LNbMO 0.02 are illustrated in Table S1 and Figures S10, S11, where LNbMO 0.02 exhibits a slight decrease in the specific surface area and pore volume compared to LMO, which is consistent with its enlarged particle size. The decreased specific surface area reduces the contact between the active material and the electrolyte, which may effectively reduce the side reactions and alleviate Mn dissolution.[46]

To investigate the effect of Nb doping on the electrochemical behavior of LMO, LNbMO with different doping amounts was tested. In Figure 2 a, cyclic voltammetry (CV) curves of all samples exhibit two pairs of well-defined redox peaks, showing that the Li^+ reversible intercalation/deintercalation process can be divided into two continuous reactions, as is shown in eqs 1−4.[47]

$$\text{Charge: } 2LiMn_2O_4 \rightarrow 2Li_{0.5}Mn_2O_4 + Li^+ + e^- \tag{1}$$

$$2Li_{0.5}Mn_2O_4 \rightarrow 4\lambda - MnO_2 + Li^+ + e^- \tag{2}$$

$$\text{Discharge: } 4\lambda - MnO_2 + Li^+ + e^- \rightarrow 2Li_{0.5}Mn_2O_4 \tag{3}$$

$$2Li_{0.5}Mn_2O_4 + Li^+ + e^- \rightarrow 2LiMn_2O_4 \tag{4}$$

This also proves that surface Nb doping does not alter the electrochemical behavior of LMO, maintaining its unique affinity to Li^+. The area enclosed by the CV curve of LNbMO 0.02 or LNbMO 0.08 is larger than that of LMO, indicating Nb doping significantly improves the electrochemical properties of LMO. The largest area of LNbMO 0.02 may correspond to the highest Li^+ storage capacity. On the contrary, the poor electrochemical performance of LNbMO 0.2 could be attributed to the excessive impurity phase on the surface of particles. Similarly, two plateaus on the charge and discharge curves in Figure 2b correspond to the two-step oxidation/reduction on the CV curves, and LNbMO 0.02 exhibits the highest capacity of 107 mAh g^{-1}. Moreover, electrochemical impedance spectroscopy (EIS) under different working potentials is performed to depict the Li^+ intercalation kinetics of LNbMO 0.02 in Figure S12, where significant difference is observed at 0.6 and 1.0 V, corresponding to distinct Li^+ diffusion (including solid-phase and liquid-phase diffusion) during the intercalation/deintercalation processes. The inset demonstrates the completion of Li^+ intercalation at 0.6 V and deintercalation at 1.0 V. In Figures 2c,d, S13, S14 and Table S2, S3, compared to LMO, LNbMO 0.02 demonstrates decreased charge-transfer resistance (R_{ct}, 3.068 Ω) and ion diffusion resistance (σ, 0.93 Ω $s^{-0.5}$) under 0.6 V. Similarly, after Nb doping, the charge-transfer resistance (R_{ct}, 1.095 Ω) and ion diffusion resistance (σ, 0.41 Ω $s^{-0.5}$) both decrease under 1.0 V. Hence, Nb doping reduces the Li^+ intercalation resistance due to the better conductivity and the broadened 3D Li^+ diffusion channel. However, LNbMO 0.08 and LNbMO 0.2 demonstrate a poor ion diffusion performance under 0.6 and 1.0 V, which can remarkably influence Li^+ diffusion in the solid phase during the Li^+ intercalation/deintercalation period. This decay could be attributed to a higher amount of impurity that hinders Li^+ transport. The diffusion coefficient can be obtained from CV tests under different scan rates in Figure S15 and Table S4, showing that the Li^+ diffusion coefficient of LNbMO 0.02 is significantly enhanced. Therefore, LNbMO 0.02 was selected as the optimal doping amount sample for the following electrochemical lithium extraction test.

In Figures 2e and S16−S18, LNbMO 0.02 exhibits two well-defined pairs of redox peaks in LiCl solution but only two oxidation peaks in the first CV cycle in $MgCl_2$ or NaCl solution without any reduction peaks, indicating that only Li^+ has the capability of intercalation into the spinel crystal structure of LNbMO 0.02. Similarly, the discharge curve in LiCl solution displays two plateaus and exhibits the highest discharge capacity compared to those in $MgCl_2$ or NaCl solutions. More importantly, the electrochemical behavior of LNbMO 0.02 in competing ions can be taken as an indicator of Li^+ selectivity, which is a key property of materials for electrochemical lithium extraction. In addition, the electrochemical cyclic stability in Figures 2f and S19,S20 shows an

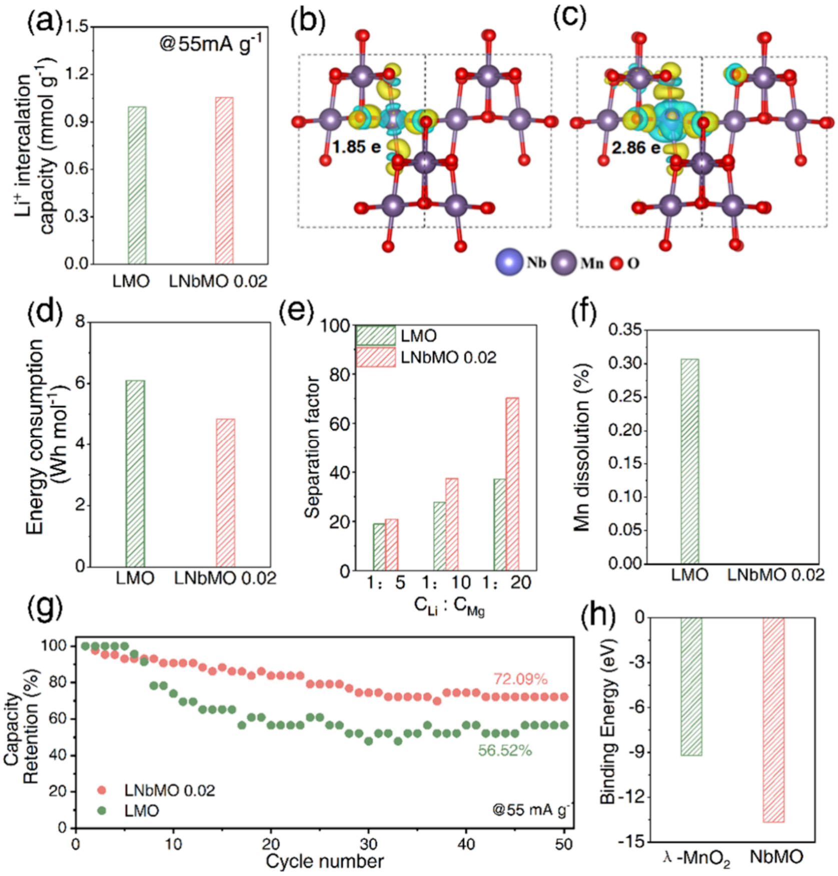

Figure 3. (a) Li$^+$ intercalation capacity of LMO and LNbMO 0.02 in 10 mM LiCl solution under −55 mA g^{-1}. (b,c) Charge density difference diagram of λ-MnO$_2$ and delithiated LNbMO (NbMO). (d) Energy consumption during the intercalation and deintercalation process. (e) Separation factors of LMO and LNbMO 0.02 in the solutions with different ratios of Li$^+$ and Mg^{2+}. (f) Percentage of Mn dissolution after the intercalation process (0 for LNbMO 0.02). (g) Li$^+$ intercalation capacity retention after 50 cycles within the cell voltage range of 0−1.0 V. (h) Binding energy of Mn−O (IV) in λ-MnO$_2$ and Nb−O in NbMO.

increased capacity retention from 34.05 to 49.42% after Nb doping, indicating the enhanced stabilization of the spinel structure and the alleviation of the Mn dissolution due to the strong bond energy of Nb−O. Thus, unlike lower-valence elements, high-valence elements as dopants have the capability of stabilizing the spinel framework without sacrificing the redox activity. The working mechanism of Li$^+$ intercalation and deintercalation during the electrochemical process is illustrated through ex situ XRD in Figure 2g−i. During the charge period from status I to IV, the characteristic peaks of LNbMO 0.02 shift to a higher 2θ degree with increasing potential, indicating lattice shrinkage and Li$^+$ deintercalation. In contrast, the characteristic diffraction peaks exhibit a peak shift to a lower 2θ degree during the discharge period from status IV to VII, revealing lattice expansion and Li$^+$ intercalation. The characteristic peaks can return to the original state, indicating the good reversibility of LNbMO 0.02 for Li$^+$ capture and release.[48]

The electrochemical lithium extraction performance is first investigated in 10 mM single Li$^+$ solution. In Figures 3a and S21, the Li$^+$ intercalation capacity gradually increases under an applied current of 55 mA g$^{-1}{}_{\text{cathode}}$, and the Li$^+$ intercalation capacity of LNbMO 0.02 reached 1.05 mmol g^{-1} after 30 min, which is slightly higher than that of LMO (0.99 mmol g^{-1}). To reveal the effect of Nb doping on increasing the Li$^+$ adsorption performance, the charge density difference is investigated in Figure 3b,c. After doping, Nb in the structure of NbMO is capable of transferring more electrons to the surrounding oxygen atoms (2.86 *e*), which is higher than that of Mn in the structure of λ-MnO$_2$ (1.85 *e*). More electrons in the surroundings of oxygen can generate a stronger electrostatic force, thus improving the Li$^+$ adsorption performance and increasing the Li$^+$ intercalation capacity.[49] The increased Li$^+$ intercalation capacity after Nb doping could also be attributed to the broadened 3D Li$^+$ diffusion channel and higher electrochemical activity from the reduced average valence of Mn. Moreover, the energy consumption during the Li$^+$ intercalation and deintercalation process is calculated in Figures 3d and S22. After Nb doping, the energy consumption effectively decreases from 6.10 to 4.83 Wh mol^{-1}, owing to the reduced Li$^+$ intercalation resistance and higher intercalation kinetics.

Given the similar radii of Li$^+$ (76 pm) and Mg^{2+} (72 pm),[50] and the high Mg/Li ratio in salt lake brine, Mg^{2+} is regarded as a significant competing cation reducing the efficiency of Li$^+$ extraction. Therefore, the Li$^+$ selectivity of electrochemical lithium extraction is first investigated in Li/Mg binary solutions. As shown in Figure 3e, the separation factors of LNbMO 0.02 are all higher than those of LMO in different molar ratios of Li$^+$/Mg^{2+}. Especially, under the condition of C(Li$^+$)/C(Mg^{2+}) = 1:20, the separation factor reaches 70.29, showing the remarkable Li$^+$ selectivity of LNbMO 0.02. Mg^{2+} may accumulate on the electrode surface driven by the electric field rather than intercalating into the bulk phase due to the high hydration energy of Mg^{2+}, which is the principal reason

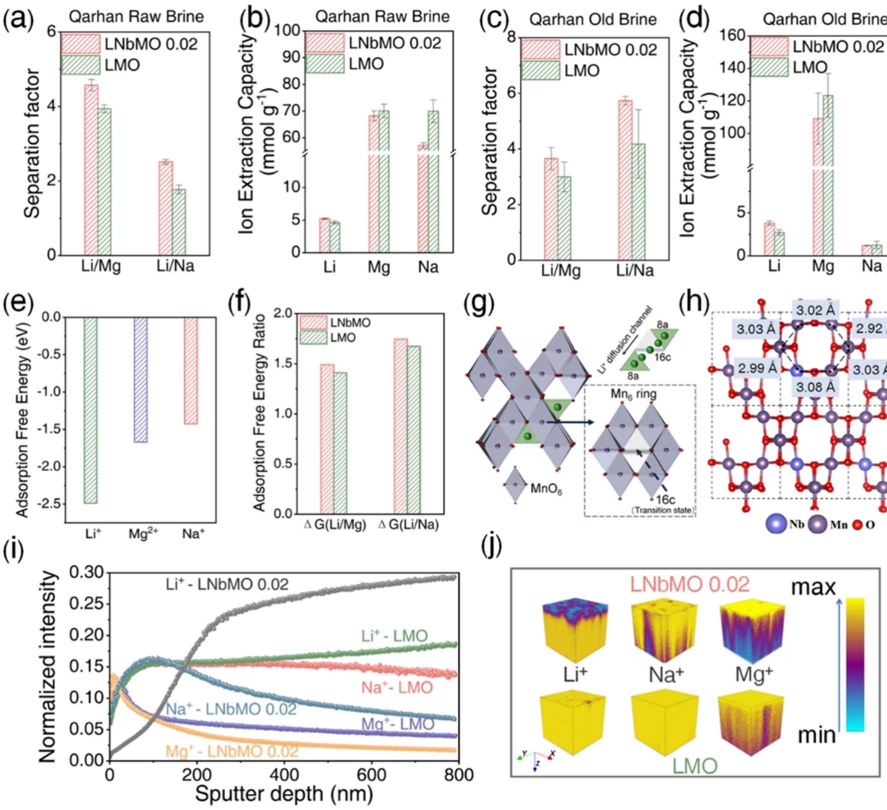

Figure 4. (a−d) Separation factor and ion extraction capacity of LMO and LNbMO 0.02 in Qarhan raw brine and old brine. (e) Adsorption free energies of Li^+, Mg^{2+}, and Na^+ on the (111) crystal plane of LNbMO. (f) Adsorption free energy ratio of Li/M^{n+} (Na^+ or Mg^{2+}) for LMO and LNbMO. (g) Schematic overview of the 3D Li^+ diffusion channel (8a-16c-8a) of spinel $LiMn_2O_4$. (h) Intermediate octahedral (16c) site (transition state) on the Li^+ diffusion channel (Mn_6 ring) of LNbMO. TOF-SIMS measurements: (i) normalized depth profile of major secondary ion species (Li^+, Mg^{2+}, Na^+) fragments of LNbMO 0.02 and LMO electrodes and (j) 3D rendering of Li^+, Na^+, and Mg^+ fragments on LNbMO 0.02 and LMO electrodes (100 μm × 100 μm × 790 nm), after electrochemical lithium extraction from Qarhan raw brine (the intensity is not normalized).

for the high Li^+ selectivity. Besides, the tuned Li^+ diffusion channel further hinders bulk phase diffusion and intercalation of Mg^{2+}. After the Li^+ intercalation, the percentage of Mn dissolution in the cathode materials is measured by ICP-OES, as shown in Figure 3f, showing no Mn dissolution of LNbMO 0.02, compared to a low Mn dissolution amount (0.31%) of LMO. Surface Nb doping of LMO effectively alleviates Mn dissolution and further stabilizes the spinel crystal structure. Additionally, the cyclic stability of active materials is also considered an essential factor. In Figures 3g and S23, the intercalation capacity retention of LNbMO 0.02 is maintained at 72.09% after 50 cycles of Li^+ intercalation and deintercalation, which is significantly higher than that of LMO (56.52%). It is consistent with the results of electrochemical cyclic stability, and the improved performance of Nb doping is related to the lower degree of Mn dissolution and stabilized crystal structure. In Figure 3h and S24, by comparing the binding energy of the specific site in spinel crystal structures before and after Nb doping, the mechanism of enhancing cyclic stability and reducing Mn dissolution of LNbMO is analyzed. The binding energy of the Nb site with oxygen atom in the NbMO structure is −13.66 eV, significantly lower than that of the Mn (IV) site in the λ-MnO_2 structure (−9.21 eV), indicating that Nb doping provides a stronger bond energy due to its strong electrostatic attraction and charge compensation effect. Furthermore, the strengthened metal−oxygen bonds and electron redistribution (reduced e_g occupancy)[51] suppress local lattice distortion and reduce the Jahn−Teller distortion of $Mn^{3+}O_6$ octahedra.[52,53] As a result, the spinel framework becomes more resistant to repeated Li^+ intercalation/deintercalation, which is beneficial to cyclic stability and reducing Mn dissolution.[54,55]

As proof of practical applications, the Nb-doped LMO is investigated in Qarhan brine, rather than simulated brine, to show the influence of Nb doping on the Li^+ selectivity of spinel LMO. The concentration ratios of Li^+/Mg^{2+} and Li^+/Na^+ reach 1:59.8 and 1:29.36 in raw brine and 1:141 and 1:2.2 in old brine, respectively. The major components of Qarhan brine are displayed in Table S5. As two major competing cations with high concentrations, Li^+ intercalation into the spinel structure is severely hindered by Na^+ and Mg^{2+}. During the electrochemical extraction process, the separation factors and ion extraction capacity of LNbMO 0.02 in Qarhan brine are compared with those of LMO in Figure 4a−d. In raw brine, LNbMO 0.02 demonstrates an enhanced separation capability of Li^+/Mg^{2+} (4.57) and Li^+/Na^+ (2.51), compared to LMO values of 3.94 and 1.77. The Li^+ extraction capacity of LNbMO 0.02 reaches 5.21 mmol g^{-1}, 13% higher than that of LMO (4.63 mmol g^{-1}). More results from the old brine show that the separation capability of LNbMO 0.02 for Li^+/Mg^{2+} (3.65) and Li^+/Na^+ (5.73) is also enhanced by Nb doping. Specifically, the Li^+ extraction capacity of LNbMO 0.02 reaches 3.79 mmol g^{-1}, compared to LMO with 2.71 mmol g^{-1}. The higher Mg^{2+} concentration in old brine seems to have an obvious influence on the Li^+ extraction capacity. In general, it can be seen that the Nb doping of LMO leads to higher Li^+ selectivity. To analyze the Li^+ selectivity of LNbMO, the ion adsorption free energy (including Li^+ and competing cations) of LNbMO is evaluated by DFT calculations in Figure 4e and S25. LNbMO exhibits a significantly low Li^+ adsorption free energy (−2.49 eV), compared to the competing Mg^{2+} (−1.67 eV) and Na^+ (−1.43 eV), revealing that Li^+ prefers to intercalate into the LNbMO crystal structure from a thermodynamic perspective. In Figure 4f, the mechanism of enhancing Li^+ selectivity after Nb doping is further analyzed. The ion adsorption free energy ratios of Li/M^{n+} (Na^+ or Mg^{2+}) after Nb doping both increase (ΔG (Li^+/Mg^{2+}) from 1.67 to 1.75 and ΔG (Li^+/Na^+) from 1.41 to 1.49), indicating that Nb doping enables the favorable intercalation of Li^+ into specific sites of the spinel structure, comparing to Mg^{2+} or Na^+.

Furthermore, the broadened 3D Li^+ diffusion channel is considered as an important factor on enhancing Li^+ selectivity. Generally, Li^+ tends to occupy the tetrahedral (8a) site, and the Li^+ diffusion pathway involves moving from a tetrahedral (8a) site to the adjacent tetrahedral (8a) site through the intermediate octahedral (16c) site (transition state), as is shown in Figure 4g. At the transition state, in particular, the Li^+ located at the octahedral 16c site is surrounded by 6 Mn ions, forming a planar Mn_6-ring perpendicular to the Li^+ diffusion channel. In Figure 4h and S26, the size of the Li^+ diffusion channel before and after Nb doping are compared. Obviously, after Nb doping, the size of the Mn_6 ring is enlarged, corresponding to the broadened 3D Li^+ diffusion channel. To further reveal the mechanism of the enhanced Li^+ selectivity after Nb doping, time-of-flight secondary ion mass spectrometry (TOF-SIMS) is conducted to analyze the compositions of the electrode surface and subsurface after electrochemical lithium extraction from Qarhan raw brine. In Figure 4i,j, the normalized depth distributions of Li^+, Mg^+, and Na^+ fragments (where the intensity of each fragment is normalized to the respective maximal intensity) on the LNbMO 0.02 and LMO electrode surfaces and 3D rendering of corresponding fragments with varying concentration at the detection depth are exhibited. It can be seen that Nb-doped LMO demonstrates a superior ionic separation capability. Na^+ and Mg^{2+} mainly accumulate on the electrode surface, and with the increased sputter depth, the intensity of Na^+ and Mg^+ fragments falls sharply, indicating a reduced concentration below the electrode surface. It is difficult for Na^+ and Mg^{2+} to diffuse in the 3D channel and intercalate into the corresponding site of the Nb-doped spinel crystal structure. Due to the higher hydration energy of Mg^{2+} (Mg^{2+} −2150 kJ mol^{-1}, Li^+ −590 kJ mol^{-1}, and Na^+ −420 kJ mol^{-1}),[56] it is extremely challenging for Mg^{2+} to dehydrate and diffuse. Thus, at about 8 nm of sputter depth, the intensity of Mg^+ fragments begins to decrease, demonstrating an ultrathin Mg^{2+} surface accumulation layer. Meanwhile, the intensity of Na^+ fragments begins to fall at about 100 nm of sputter depth, indicating the bulk diffusion of Na^+, and it originates from the extremely large concentration differences and facile Na^+ dehydration. The results reflect that Na^+ is more competitive than Mg^{2+} under high salt conditions, which also explains the lower separation factor of Li/Na than that of Li/Mg in raw brine. However, considering the large ionic radii of Na^+ (102 pm)[57] and poor adsorption free energy of Na^+, its diffusion in the ion transport channel and intercalation into the 8a site would become more difficult, which also explains the reduction of Na^+ intensity with increasing depth. In contrast, the intensity of Li^+ fragment rises with the increased depth, indicating the occurrence of competitive adsorption or intercalation on the surface and subsurface, and the prominent ability of Li^+ intercalation into the 8a site of the Nb-doped spinel crystal structure via the broadened 3D diffusion channel.

As for the control group, the ionic separation capability of the LMO is not impressive. No significant decline of Na^+ and Mg^+ fragments intensity can be spotted with the increasing sputter depth. At about 790 nm of sputter depth, the intensity of Na^+ fragments is still maintained at a high level, revealing the severe bulk diffusion of Na^+ on the LMO electrode. Similarly, the bulk diffusion of Mg^{2+} is more obvious in the LMO electrode. This confirms the positive effect of Nb doping on diminishing the bulk diffusion of Na^+ and Mg^{2+} in the spinel crystal structure. The local charge density distribution changes due to Nb doping, which may reduce the affinity between the diffusion channel and competing cations. The normalized Li^+ fragment intensity increases slightly with depth, which can be attributed to the severe Na^+ and Mg^{2+} bulk diffusion hindering Li^+ intercalation into the spinel structure and diffusion to deeper regions. The diffusion of competing cations in the bulk phase may reduce Li^+ diffusion and intercalation, resulting in the reduction of the Li^+ selectivity. Therefore, this evidence emphasizes the importance of a broadened Li^+ diffusion channel created by Nb doping. Although the size of the Li^+ diffusion channel is enlarged after Nb doping, the dehydration of Mg^{2+} (high hydration energy) and the diffusion of Na^+ (large ionic radii) are still challenging. In other words, the Li^+ diffusion channel has no negative effect on diminishing the bulk diffusion of competing cations; however, by tuning the diffusion channel, the channel polarity favors Li^+ over competing cations. The broadened 3D channel reduces the Li^+ migration barrier, facilitating the diffusion of Li^+ while increasing the diffusion barrier of competing cations, retarding the diffusion of competing cations. In short, the mechanism of enhanced Li^+ selectivity after Nb doping is mainly interpreted as an increasing preference of Li^+ intercalation into specific sites, reducing the Li^+ diffusion barrier and enhancing the affinity between Li^+ and the diffusion channel via tuning the diffusion channel. In addition, other representative competing cation fragments, including K^+, Ca^+, and B^+, are also exhibited in Figure S27−S29, showing a stronger ion separation capability of LNbMO 0.02. The uniform distribution of Nb^+ fragments in the LNbMO 0.02 electrode also verifies the successful doping of Nb.

More importantly, a two-step intermittent operation is conducted in Qarhan raw brine to assess the practical application of Nb-doped LMO in electrochemical lithium extraction. The schematic diagram of the two-step intermittent operation is illustrated in Figure 5a. First, under an applied current of −55 mA $g^{-1}{}_{cathode}$, the delithiated LNbMO 0.02 captures Li^+ from the Qarhan raw brine, while other competing cations accumulate on the electrode surface and anion-exchange membrane or even cointercalate into the electrode. On the anode, activated carbon captures anions across the anion-exchange membrane (mostly Cl^-). After the Li^+ capture step, flushing the cell, including the electrode surfaces and membrane, is a key procedure to remove residual competing cations. The cleansing agent selected is deionized water and 10 mM NaCl solution, and the law of choice is illustrated below. Then, for the Li^+ release step, under a reversed applied current

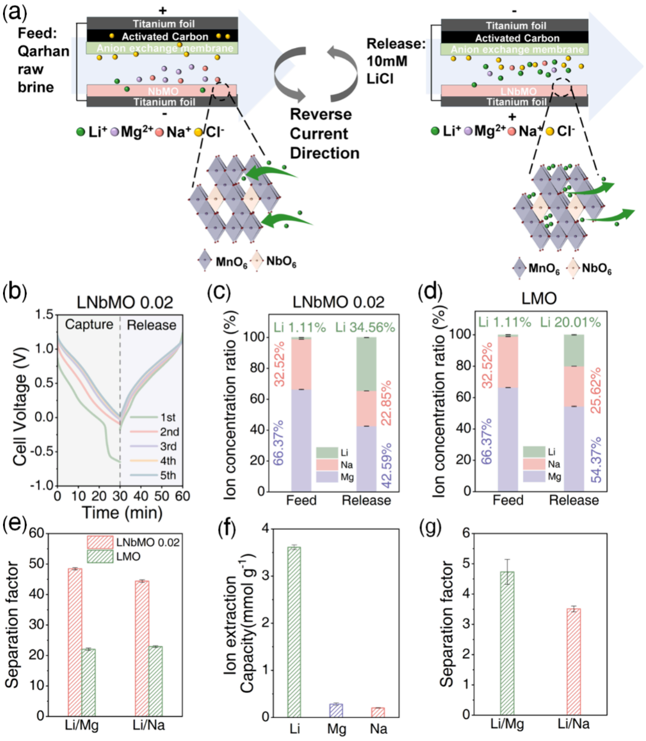

Figure 5. (a) Schematic diagram of two-step intermittent operation for electrochemical lithium extraction from Qarhan raw brine by LNbMO. (b) Cell voltage variation of the LNbMO||AC configuration in 5 cycles of two-step intermittent operation. (c,d) Composition in the receiving solution after lithium electrochemical lithium extraction by LNbMO 0.02 and LMO (the lithium content has ruled out the 10 mM lithium that originally existed in the receiving solution). (e) Separation factor after 5 cycles of electrochemical lithium extraction from Qarhan raw brine (the lithium content has ruled out the 10 mM lithium that originally existed in the receiving solution). (f) Ion extraction capacity of LNbMO 0.02 during the secondary extraction process. (g) Separation factor of LNbMO 0.02 during the secondary extraction process.

of 55 mA $g^{-1}_{cathode}$, Li^+ can be released from the LNbMO 0.02 electrode into the receiving solution (10 mM LiCl), achieving the enrichment of Li^+ from raw brine. As shown in Figures 5b and S30, the cell voltage decreases at the Li^+ capture stage, while at the Li^+ release stage, the cell voltage gradually increases. The two-step intermittent operation is repeated for 5 cycles, and the major components in the receiving solution are displayed in Figure 5c,d. The ion concentration ratio of Li^+ increases from 1.11% in Qarhan raw brine to 34.56% in the receiving solution after capture and release steps by LNbMO 0.02, while it is only 20.01% in the receiving solution by LMO. The contents of Mg^{2+} and Na^+ show an obvious reduction in the receiving solution, indicating the superior Li^+ selectivity and realizing efficient initial Li^+ enrichment by Nb doping. The Li^+ selectivity of the two-step intermittent operation is also defined by the separation factor in Figure 5e. The separation capability of LMO for Li^+/Mg^{2+} is 22.05 and that for Li^+/Na^+ is 22.93. By Nb doping, the separation factor of Li^+/Mg^{2+} and Li^+/Na^+ increases to 48.47 and 44.42, respectively, effectively achieving the selective Li^+ extraction from real brine. Compared to previous research shown in Table S6, this diffusion channel engineering via a high-valent Nb doping strategy proves to be viable and robust for electrochemical lithium extraction from low-grade brines.

The significant difference before and after Nb doping can also be explained by Figure 4e,f and i,j. More Li^+ has the superior ability of a thermodynamically favorable intercalation into the corresponding site and diffusion to a deeper region with Nb doping, reducing the possible Li^+ loss during the flushing process. The removal rate with deionized water flushing of Mg^{2+} is significantly higher than that with Na^+ during the flushing process, which can be attributed to more surface accumulation and less bulk diffusion of Mg^{2+}. Thus, Mg^{2+} can be removed more easily during the flushing process, while the removal of Na^+ becomes difficult due to the severe bulk diffusion. To further enhance the purity of Li^+ from the LNbMO 0.02||AC cell, secondary Li^+ extraction from the receiving solution is performed, as shown in Figure 5f,g. The Li^+ extraction capacity reaches 3.61 mmol g^{-1} in the receiving solution, much higher than those of Mg^{2+} (0.28 mmol g^{-1}) and Na^+ (0.20 mmol g^{-1}). The separation factors of the secondary Li^+ extraction process for Li^+/Mg^{2+} and Li^+/Na^+ are 4.73 and 3.51, respectively. More interestingly, the selection of cleansing agents during the flushing stage is also explored as a key issue. If deionized water alone acts as the cleansing agent, the performance for the two-step intermittent operation of LNbMO 0.02||AC cell in Qarhan raw brine is demonstrated in Figure S31–S34. The ratio of Li^+ slightly increases from 1.11 to 11.12% in the receiving solution, revealing that the Li^+ extraction efficiency is far lower than the condition of using 10 mM NaCl. The separation factors of Li^+/Mg^{2+} and Li^+/Na^+ also seriously decrease (Li^+/Mg^{2+} 11.12 and Li^+/Na^+ 11.28), compared to the ones with 10 mM NaCl. To figure out the possible cause of the positive effect from 10 mM NaCl on the flushing process, more experimental details are described in the Supporting Information, and the corresponding results are displayed in Figure S35–S37. Compared to mixing with NaCl solution, simply using deionized water has the difficulty of effectively removing the accumulated impurity cations on the surface of the AEM, further affecting the efficiency of electrochemical lithium extraction. Furthermore, AEM was characterized after five cycles of two-step intermittent operation in the Qarhan raw brine, showing that the contents of Mg^{2+}, Na^+, and K^+ on the used AEM all increased, indicating the accumulation of competing cations, as shown in Figures S38, S39 and Table S7, S8. In addition, in Figure S40, the ionic conductivity decreased, which also verified the negative impact of membrane fouling on its performance and efficiency. Therefore, the fouling of AEM caused by high-salinity brine is a key issue for electrochemical lithium extraction, and it needs to be further explored via membrane experts.

CONCLUSIONS

In general, we developed a diffusion-channel-engineered spinel LMO cathode via Nb doping that exhibits a superior electrochemical lithium extraction performance. Nb incorporation simultaneously increases the lattice constant, reduces the Mn valence, and strengthens Mn–O bonding, thereby lowering the Li^+ diffusion resistance and improving the structural stability. As a result, the Nb-doped LMO achieves a high discharge capacity of 107 mA g^{-1}, a reduced energy consumption of 4.83 Wh mol^{-1} Li^+, and superior cycling stability with a high-capacity retention of 72.09% after 50 cycles. Crucially, the strategy proves effective in real Qarhan brine, where Nb-doped LMO exhibits high Li^+ extraction capacity (5.21 mmol g^{-1} in raw brine and 3.79 mmol g^{-1} in old brine), outstanding Li^+ selectivity (Li^+/Mg^{2+} = 48.47 and Li^+/Na^+ = 44.42), and excellent enrichment capability, raising the Li^+ concentration ratio from 1.11% in raw brine to 34.56% in the receiving solution. TOF-SIMS and DFT analyses reveal that the broadened diffusion channel not only favors Li^+ intercalation thermodynamically but also kinetically suppresses the bulk diffusion of competing cations. By demonstrating a high-valent doping strategy for diffusion channel engineering, this study paves the way for scalable, sustainable lithium recovery from complex brines and advances electrochemical separation technologies.

MATERIALS AND METHODS

Materials Synthesis. Nb-doped $LiMn_2O_4$ ($LiNb_xMn_{2-x}O_4$, x = 0, 0.02, 0.08, 0.2) was prepared by solid-state reaction. EMD, Li_2CO_3, and Nb_2O_5 were weighted according to the exact molar ratio and ground in a mortar for 30 min. The mixed powder was stirred for 30 min in ethanol and dried at 120 °C. Subsequently, the mixed powder was calcinated from room temperature to 600 °C at a rate of 8 °C/min and kept at 600 °C for 10 h and then calcinated from 600 to 750 °C at a rate of 8 °C/min and kept at 8 h, where the calcination atmosphere was N_2. The products were denoted as LMO, LNbMO 0.02, LNbMO 0.08, and LNbMO 0.2, respectively.

Electrochemical Lithium Extraction. Before the electrochemical lithium extraction, LNbMO (or LMO) needs to be delithiated under a potential of 0.8 V (vs Ag/AgCl) for 10 min and then at 1.0 V (vs Ag/AgCl) for 110 min to obtain delithiated LNbMO (or delithiated LMO). The electrochemical lithium extraction was performed under a constant current operation mode, in which LNbMO (or LMO) was used as the cathode material and activated carbon (AC) was used as the anode material. Additionally, an anion-exchange membrane (AEM) was assembled between the cathode and the anode. A flow-through cell was used for electrochemical lithium extraction experiments by cycling 60 mL of solution at 15 mL min^{-1} with a peristaltic pump. In a single-ion extraction experiment, the current of ± 55 mA $g^{-1}{}_{cathode}$ was applied for 30/30 min for Li^+ intercalation (discharge)/deintercalation (charge), where 10 mM LiCl solution was used as the electrolyte. ICP-OES (Thermo Fisher iCAP PRO) was performed to determine the ion concentration variation and the Li^+ intercalation capacity (Γ, mmol g^{-1}), which was calculated by eq 5:

$$\Gamma = \frac{(C_0 - C_i)V}{m} \tag{5}$$

where C_0 and C_i (mmol L^{-1}) are the initial and the final Li^+ concentrations, respectively. V (L) is the volume of the electrolyte and m (g) is the mass of active material in the LNbMO (or LMO) electrode.

A long cycle Li^+ extraction experiment was performed under ± 55 mA $g^{-1}{}_{cathode}$, and the cut-off voltage was between 0 and 1.0 V. The Li^+ concertation was monitored by a conductivity meter (S230, Mettler Toledo). The dissolved Mn content of the cathode material was also determined by ICP-OES, and the percentage of Mn dissolution was calculated by eq 6:

$$\text{Mn dissolution \%} = \frac{C \cdot V}{w \cdot m} \tag{6}$$

where C is the dissolved Mn^{2+} concentration (g L^{-1}), V (L) is the volume of electrolyte, m (g) is the mass of active material in the LNbMO (or LMO) electrode, and w is the corresponding mass fraction of Mn in LNbMO (or LMO).

The energy consumption (W, Wh mol^{-1}) can be calculated by eq 7:

$$W = \frac{\oint \Delta V \mathrm{d}q}{3600 Q_{Li}} \tag{7}$$

where ΔV (V) is the cell voltage window during the intercalation/deintercalation process and q (C g^{-1}) is the charge amount per gram of the active material in the cathode electrode.

The Li^+/Mg^{2+} selective extraction experiment was performed under ±55 mA $g^{-1}{}_{cathode}$ for 30 min intercalation /30 min deintercalation, where a binary solution containing Li^+ and Mg^{2+} with different Li^+/Mg^{2+} molar ratios (10:50, 10:100, and 10:200 mM) were used. The variation of the ion concentration was also determined by ICP-OES (Thermo Fisher iCAP PRO). The separation factor was used to evaluate the selectivity for Li^+ (βLi M). βLi M is the ratio of the intercalation percentage for Li^+ to the intercalation percentage for Mg^{2+}. The ion intercalation percentage and βLi+ Mg2 based on the extraction process can be calculated by eqs 8 and 9:

$$\text{Ion intercalation percentage} = \frac{C_0 - C_i}{C_0} \tag{8}$$

$$\beta_{M}^{Li} = \frac{\text{Removal percentage } (Li^+)}{\text{Removal percentage } (M)} \tag{9}$$

where C_0 (mol g^{-1}) and C_i (mol g^{-1}) are the initial and final concentrations of the ion, respectively, and M denotes the impurity cations (Na^+, Mg^{2+}).

Similarly, the selective experiments in Qarhan raw brine and Qarhan old brine were operated under the same conditions as above. Due to the high content and strong interfering effect of Na^+ and Mg^{2+}, the evaluation of the Nb-doped LMO separation property primarily involved Li^+, Na^+ and Mg^{2+}, and the results can be obtained according to eqs 8 and 9.

Finally, the two-step intermittent operation for electrochemical lithium extraction, including Li^+ capture (intercalation) and release (deintercalation), was conducted in Qarhan raw brine, in which the received solution was 10 mM LiCl. The concentrations of Li^+, Na^+, and Mg^{2+} in the received solution were also determined by ICP-OES to comprehensively evaluate the electrochemical lithium extraction properties of Nb-doped LMO. The ion concentration ratio in the received solution can be calculated according to eq 10:

$$\text{Ion concentration ratio} = \frac{C_{M-release}}{C_{Li-release} + C_{Mg-release} + C_{Na-release}} \times 100\% \tag{10}$$

where $C_{M\text{-}release}$ represents any metal (Li^+, Mg^{2+}or Na^+) ion molar concentration (mmol L^{-1}) in the corresponding received solution, in which $C_{Li\text{-}release}$ does not take into account the 10 mM lithium that originally existed in the receiving solution.

The Li^+ selectivity based on two steps intermittent operation can be calculated by eq 11:

$$\alpha_{M}^{Li} = \frac{C_{Li-release}/C_{M-release}}{C_{Li-feed}/C_{M-feed}} \tag{11}$$

where $C_{Li\text{-}release}$ and $C_{M\text{-}release}$ represent the ion concentrations (mg/L) of Li^+ (not including initial 10 mM LiCl) and M (Na^+ and Mg^{2+}) in the received solution, respectively. $C_{Li-feed}$ and C_{M-feed} are the ion concentrations (mg L^{-1}) in Qarhan raw brine, respectively.

Detailed electrode fabrication, materials characterization, and electrochemical measurements and DFT calculation are described in the Supporting Information.

ASSOCIATED CONTENT

Data Availability Statement

The data supporting this article have been included as part of the Supporting Information.

Supporting Information

The Supporting Information is available free of charge at https://pubs.acs.org/doi/10.1021/acsnano.5c14948.

Additional experimental details, materials, and methods; characterization data; electrochemical testing results;

electrochemical lithium extraction data; supplementary tables, figures, and references (PDF)

AUTHOR INFORMATION

Corresponding Authors

Yang Wang − *School of Chemical Engineering and Technology and National Industry-Education Integration Platform of Energy Storage, Tianjin University, Tianjin 300350, China; Tianjin Key Laboratory of Membrane Science and Desalination Technology, Tianjin 300072, China;* orcid.org/0000-0003-1928-2506; Email: yangwang2017@tju.edu.cn

Jieshan Qiu − *College of Chemical Engineering, Beijing University of Chemical Technology, Beijing 100029, China;* Email: qiujs@mail.buct.edu.cn

Authors

Yixuan Qiao − *School of Chemical Engineering and Technology, Tianjin University, Tianjin 300350, China*

Houjun Zhang − *School of Chemical Engineering and Technology, Tianjin University, Tianjin 300350, China*

Yao Nian − *School of Chemical Engineering and Technology and National Industry-Education Integration Platform of Energy Storage, Tianjin University, Tianjin 300350, China;* orcid.org/0000-0001-7999-7437

Yuqi Li − *School of Chemical Engineering and Technology, Tianjin University, Tianjin 300350, China;* orcid.org/0009-0009-4959-7200

Changwei Xiao − *School of Chemical Engineering and Technology, Tianjin University, Tianjin 300350, China*

Tiantian Wang − *School of Chemical Engineering and Technology, Tianjin University, Tianjin 300350, China*

Mingjian Wen − *Institute of Fundamental and Frontier Sciences, University of Electronic Science and Technology of China, Chengdu 611731, China;* orcid.org/0000-0003-0013-575X

You Han − *School of Chemical Engineering and Technology and National Industry-Education Integration Platform of Energy Storage, Tianjin University, Tianjin 300350, China;* orcid.org/0000-0002-6903-0844

Complete contact information is available at:
https://pubs.acs.org/10.1021/acsnano.5c14948

Notes

The authors declare no competing financial interest.

ACKNOWLEDGMENTS

This work was supported by the National Natural Science Foundation of China (No. 22178253) and the Tianjin Metrology Technology Project (No. 2024TJMT038).

REFERENCES

(1) Wang, W.; Liu, Z.; Zhu, Z.; Ma, Y.; Zhang, K.; Meng, Y.; Ahmad, T.; Khan, N. A.; Peng, Q.; Xie, Z.; Zhang, Z.; Chen, W. Electrochemical lithium recycling from spent batteries with electricity generation. *Nat. Sustainability* **2025**, 287.

(2) Yang, S.; Wang, Y.; Pan, H.; He, P.; Zhou, H. Lithium extraction from low-quality brines. *Nature* **2024**, *636* (8042), 309−321.

(3) Yan, G.; Wang, M.; Hill, G. T.; Zou, S.; Liu, C. Defining the challenges of Li extraction with olivine host: The roles of competitor and spectator ions. *Proc. Natl. Acad. Sci. U. S. A.* **2022**, *119* (31), No. e2200751119.

(4) Xu, J.; Jin, Y.; Liu, K.; Lyu, N.; Zhang, Z.; Sun, B.; Jin, Q.; Lu, H.; Tian, H.; Guo, X.; Shanmukaraj, D.; Wu, H.; Li, M.; Armand, M.; Wang, G. A green and sustainable strategy toward lithium resources recycling from spent batteries. *Sci. Adv.* **2022**, *8* (40), No. eabq7948.

(5) Kong, L.; Yan, G.; Hu, K.; Yu, Y.; Conte, N.; McKenzie, K. R.; Wagner, M. J.; Boyes, S. G.; Chen, H.; Liu, C.; Liu, X. Electro-driven direct lithium extraction from geothermal brines to generate battery-grade lithium hydroxide. *Nat. Commun.* **2025**, *16* (1), 806.

(6) Feng, Y.; Park, Y.; Hao, S.; Fang, Z.; Terlier, T.; Zhang, X.; Qiu, C.; Zhang, S.; Chen, F.; Zhu, P.; Nguyen, Q.; Wang, H.; Biswal, S. L. Three-chamber electrochemical reactor for selective lithium extraction from brine. *Proc. Natl. Acad. Sci. U. S. A.* **2024**, *121* (47), No. e2410033121.

(7) Li, X.; Yao, Y.; Guo, B.; Wu, W.; Lu, S.; Qin, W.; Wu, X. Fe(III)/Fe(II) Redox-Based Lithium Extraction/Recovery from Liquid- and Solid-Phase Lithium Resources. *ACS Energy Letters* **2024**, *9* (2), 758−767.

(8) Li, Z.; Chen, I. C.; Cao, L.; Liu, X.; Huang, K.-W.; Lai, Z. Lithium extraction from brine through a decoupled and membrane-free electrochemical cell design. *Science* **2024**, *385* (6716), 1438−1444.

(9) Bing, S.; Xian, W.; Chen, S.; Song, Y.; Hou, L.; Liu, X.; Ma, S.; Sun, Q.; Zhang, L. Bio-inspired construction of ion conductive pathway in covalent organic framework membranes for efficient lithium extraction. *Matter* **2021**, *4* (6), 2027−2038.

(10) Sun, K.; Tebyetekerwa, M.; Zeng, X.; Wang, Z.; Duignan, T. T.; Zhang, X. Understanding the Electrochemical Extraction of Lithium from Ultradilute Solutions. *Environ. Sci. Technol.* **2024**, *58* (8), 3997−4007.

(11) Zhang, S.; Wei, X.; Cao, X.; Peng, M.; Wang, M.; Jiang, L.; Jin, J. Solar-driven membrane separation for direct lithium extraction from artificial salt-lake brine. *Nat. Commun.* **2024**, *15* (1), 238.

(12) Liu, C.; Li, Y.; Lin, D.; Hsu, P.-C.; Liu, B.; Yan, G.; Wu, T.; Cui, Y.; Chu, S. Lithium Extraction from Seawater through Pulsed Electrochemical Intercalation. *Joule* **2020**, *4* (7), 1459−1469.

(13) Zhang, G.; Li, Y.; Guan, X.; Hu, G.; Su, H.; Xu, X.; Feng, G.; Shuchi, S. B.; Kim, S. C.; Zhou, J.; Xu, R.; Xiao, X.; Wu, A.; Cui, Y. Spontaneous lithium extraction and enrichment from brine with net energy output driven by counter-ion gradients. *Nature Water* **2024**, *2* (11), 1091−1101.

(14) Peng, Q.; Wang, R.; Zhao, Z.; Lin, S.; Liu, Y.; Dong, D.; Wang, Z.; He, Y.; Zhu, Y.; Jin, J.; Jiang, L. Extreme Li-Mg selectivity via precise ion size differentiation of polyamide membrane. *Nat. Commun.* **2024**, *15* (1), 2505.

(15) Wu, X.; Zhang, H.; Zhang, X.; Guan, Q.; Tang, X.; Wu, H.; Feng, M.; Wang, H.; Ou, R. Sustainable lithium extraction enabled by responsive metal-organic frameworks with ion-sieving adsorption effects. *Proc. Natl. Acad. Sci. U. S. A.* **2024**, *121* (6), No. e2309852121.

(16) Li, H.; Pan, J.; Ping, Y.; Su, J.; Fang, M.; Chen, T.; Pan, B.; Lu, Z. Annealed SiO(2) Protective Layer on LiMn(2)O(4) for Enhanced Li-Ion Extraction from Brine. *Nano Lett.* **2023**, *23* (22), 10458−10465.

(17) Su, H.; Li, Z.; Zhang, J.; Liu, W.; Zhu, Z.; Wang, L.; Qi, T. Combining Selective Extraction and Easy Stripping of Lithium Using a Ternary Synergistic Solvent Extraction System through Regulation of Fe3+ Coordination. *ACS Sustainable Chem. Eng.* **2020**, *8* (4), 1971−1979.

(18) Battistel, A.; Palagonia, M. S.; Brogioli, D.; La Mantia, F.; Trocoli, R. Electrochemical Methods for Lithium Recovery: A Comprehensive and Critical Review. *Adv. Mater.* **2020**, *32* (23), No. e1905440.

(19) Zhang, H.; Zhao, L.; Guo, Z.; Wang, L.; Ma, Y.; Zhang, P.; Wang, J.; Ji, Z.-Y. Ultrashort and Vertically Aligned Channels: Boosted Lithium Selective Extraction via Hybrid Capacitive Deionization. *Environ. Sci. Technol.* **2025**, 6881.

(20) Hill, G. T.; Shi, F.; Zhou, H.; Han, Y.; Liu, C. Layer spacing gradient (NaLi)1−xCoO2 for electrochemical Li extraction. *Matter* **2021**, *4* (5), 1611−1624.

(21) Zeng, Y.; Li, W.; Wan, Z.; Qin, S.; Huang, Q.; Cai, W.; Wang, Q.; Yao, M.; Zhang, Y. Electrochemically Mediated Lithium Extraction for Energy and Environmental Sustainability. *Adv. Funct. Mater.* **2024**, 2400416.

(22) Zhao, X.; Yang, S.; Song, X.; Wang, Y.; Zhang, H.; Li, M.; Wang, Y. Enhanced Lithium Extraction from Brines: Prelithiation Effect of FePO4 with Size and Morphology Control. *Adv. Sci.* **2024**, *11* (41), No. 2405176.

(23) Bao, Y.; Ji, Z.; Zhou, H.; Zhang, C.; Song, S.; Jia, F.; Li, J.; Quintana, M. Li-Ions Pre-intercalation Strategy of Manganese Oxides for Capacitive Deionization-Based Selective Lithium Extraction From Low-grade Brine. *Small* **2024**, No. 2406951.

(24) Wang, Z.; Chen, Z.; Li, Y.; Ren, X.; Xiong, X.; Lu, Z.; Deng, L. Photothermal-enhanced ion transport for efficient electrochemical lithium extraction at low temperatures. *Nano Energy* **2024**, *131*, No. 110249.

(25) Wan, Z.; Liu, Z.; Xiao, Y.; Ruan, Q.; Wang, Q.; Zhang, H.; Yao, M.; Zhang, Y. Self-Oxidated Hybrid Conductive Network Enables Efficient Electrochemical Lithium Extraction Under High-Altitude Environment. *Small* **2024**, No. e2406607.

(26) Ma, G.; Xu, Y.; Cai, A.; Mao, H.; Zhang, X.; Shin, D. M.; Wang, L.; Zhou, H. Binder-Free LiMn(2) O(4) Nanosheets on Carbon Cloth for Selective Lithium Extraction from Brine via Capacitive Deionization. *Small* **2024**, *20* (9), No. e2306530.

(27) Wang, Y.; Zhang, J.; Cheng, Z.; Xiang, X. Hydrophilic Modification Using Polydopamine on Core−Shell Li1.6Mn1.6O4@ Carbon Electrodes for Lithium Extraction from Lake Brine. *ACS Sustainable Chem. Eng.* **2022**, *10* (27), 8970−8979.

(28) Weng, D.; Duan, H.; Hou, Y.; Huo, J.; Chen, L.; Zhang, F.; Wang, J. Introduction of manganese based lithium-ion Sieve-A review. *Progress in Natural Science: Materials International* **2020**, *30* (2), 139−152.

(29) Meng, X.; Bi, Z.; Lou, P.; Shang, G. Tracking Electrochemical-Cycle-Induced Surface Structure Evolutions of Cathode Material LiMn2O4 with Improved Operando Raman Spectroscopy. *Langmuir* **2022**, *38* (12), 3887−3895.

(30) Huang, Y.; Dong, Y.; Li, S.; Lee, J.; Wang, C.; Zhu, Z.; Xue, W.; Li, Y.; Li, J. Lithium Manganese Spinel Cathodes for Lithium-Ion Batteries. *Adv. Energy Mater.* **2020**, *11* (2), No. 2000997.

(31) An, X.; Du, Z.; Qiao, B.; Wang, S.; Wang, P.; Ma, X.; Li, Y.; Du, X.; Hao, X.; Guan, G. Co-doping induced Mn-vacancy LiMn2O4 based membrane electrode for lithium extraction by electrochemically switched ion permselective process. *Desalination* **2024**, *591*, No. 118016.

(32) Meng, X.; Jing, Y.; Li, J.; Sun, Z.; Wu, Z. Electrochemical recovery of lithium from brine by highly stable truncated octahedral LiNi0.05Mn1.95O4. *Chem. Eng. Sci.* **2024**, *283*, No. 119400.

(33) Tian, G.; Gao, J.; Yan, S.; Wang, H.; Li, R.; Xiang, J.; Du, W.; Zhang, L.; Tang, N. Long-acting electrochemical lithium-recovery from original brine using super-stable spinel lithium manganate oxide. *Desalination* **2024**, *592*, No. 118103.

(34) Shang, X.; Hu, B.; Nie, P.; Shi, W.; Hussain, T.; Liu, J. LiNi0.5Mn1.5O4-based hybrid capacitive deionization for highly selective adsorption of lithium from brine. *Sep. Purif. Technol.* **2021**, *258*, No. 118009.

(35) Wu, Y.; Shi, P.; Zhong, Y.; Cai, R. Improved Performance of a Ni, Co-Doped LiMn2O4 Electrode for Lithium Extraction from Brine. *Energy Fuels* **2023**, *37* (5), 4083−4093.

(36) Tian, G.; Gao, J.; Wang, M.; Wen, X.; Liu, Y.; Xiang, J.; Zhang, L.; Cheng, P.; Zhang, J.; Tang, N. Structural stabilization of Cr-doped spinel LiMn2O4 for long-term cyclability towards electrochemical lithium recovery in original brine. *Electrochim. Acta* **2024**, *475*, No. 143361.

(37) Tan, G.; Wan, S.; Chen, J. J.; Yu, H. Q.; Yu, Y. Reduced Lattice Constant in Al-Doped LiMn(2)O(4) Nanoparticles for Boosted Electrochemical Lithium Extraction. *Adv. Mater.* **2024**, *36* (14), No. e2310657.

(38) Sun, X.; Xiao, R.; Yu, X.; Li, H. Screening LiMn(2)O(4) Surface Modification Schemes under Theoretical Guidance. *ACS Appl. Mater. Interfaces* **2022**, *14* (8), 10353−10362.

(39) Zhan, C.; Wu, T.; Lu, J.; Amine, K. Dissolution, migration, and deposition of transition metal ions in Li-ion batteries exemplified by Mn-based cathodes − a critical review. *Energy Environ. Sci.* **2018**, *11* (2), 243−257.

(40) Wang, S.; Yang, J.; Wu, X.; Li, Y.; Gong, Z.; Wen, W.; Lin, M.; Yang, J.; Yang, Y. Toward high capacity and stable manganese-spinel electrode materials: A case study of Ti-substituted system. *J. Power Sources* **2014**, *245*, 570−578.

(41) Zhang, J.; Ma, L.; Hai, C.; Chen, T.; Gao, Y.; Xu, Y.; Pan, W.; Chen, J.; Sun, Y.; Dong, S.; He, X.; Xu, Q.; Wu, X.; Quan, C.; Su, H.; Zhou, Y. Enhancing hydrophilicity of thick electrodes via sulfonation reaction for lithium extraction from salt lake. *Desalination* **2025**, *604*, No. 118669.

(42) Mao, J.; Dai, K.; Xuan, M.; Shao, G.; Qiao, R.; Yang, W.; Battaglia, V. S.; Liu, G. Effect of Chromium and Niobium Doping on the Morphology and Electrochemical Performance of High-Voltage Spinel LiNi0.5Mn1.5O4 Cathode Material. *ACS Appl. Mater. Interfaces* **2016**, *8* (14), 9116−9124.

(43) Li, X.; Xu, Y. Spinel LiMn2O4 active material with high capacity retention. *Appl. Surf. Sci.* **2007**, *253* (21), 8592−8596.

(44) Su, Y.; Qian, F.; Qian, Z. Enhancing adsorption capacity and structural stability of Li1.6Mn1.6O4 adsorbents by anion/cation co-doping. *RSC Adv.* **2022**, *12* (4), 2150−2159.

(45) Li, G.; Chen, X.; Yu, Y.; Zhang, B.; Yang, W. Synthesis of high-energy-density LiMn2O4 cathode through surficial Nb doping for lithium-ion batteries. *J. Solid State Electrochem.* **2018**, *22* (10), 3099−3109.

(46) Wang, L.-F.; Ou, C.-C.; Striebel, K. A.; Chen, J.-S. Study of Mn Dissolution from LiMn2 O 4 Spinel Electrodes Using Rotating Ring-Disk Collection Experiments. *J. Electrochem. Soc.* **2003**, *150* (7), A905.

(47) Xue, N.; Zhang, Y.; Wu, X.; Yu, J.; Zhang, Y.; Wei, R.; Yu, Y.; Cui, Y.; Liu, W. Stable Electrochemical Lithium Extraction Using LiMn2O4 Coated With Lithiated Nafion. *Small Methods* **2025**, No. e2401972.

(48) Luo, G.; Zhou, M.; Chao, Y.; Cui, P.; Li, X.; Chen, L.; Jiang, G.; Zhu, W.; Liu, Z.; Xu, C. Augmented electrochemical extraction lithium performance via interface alloying modification. *Sep. Purif. Technol.* **2025**, *354*, No. 128683.

(49) Moreno-Castilla, C.; Alvarez-Merino, M. A.; Pastrana-Martinez, L. M.; Lopez-Ramon, M. V. Adsorption mechanisms of metal cations from water on an oxidized carbon surface. *J. Colloid Interface Sci.* **2010**, *345* (2), 461−466.

(50) Wei, S.; Wei, Y.; Chen, T.; Liu, C.; Tang, Y. Porous lithium ion sieves nanofibers: General synthesis strategy and highly selective recovery of lithium from brine water. *Chem. Eng. J.* **2020**, *379*, No. 122407.

(51) Yang, N.; You, Y.; Ou, S.; Wang, L.; Li, Z.; Xu, J.; Luo, H.; Yuan, M. Nb5+ doping modulates crystal morphology and electronic structure of spinel LiMn2O4 for high-rate long-cycle cathode materials. *Particuology* **2025**, *106*, 236−247.

(52) Lee, Y. K.; Park, J.; Lu, W. Electronic and Bonding Properties of LiMn2O4Spinel with Different Surface Orientations and Doping Elements and Their Effects on Manganese Dissolution. *J. Electrochem. Soc.* **2016**, *163* (7), A1359−A1368.

(53) Ramogayana, B.; Santos-Carballal, D.; Maenetja, K. P.; Malatji, K. T.; de Leeuw, N. H.; Ngoepe, P. E. A DFT + U-D3 Study of the Adsorption of Hydrogen Fluoride and Ethylene Carbonate on the Niobium-Doped (001), (011), and (111) Surfaces of Lithium Manganese Oxide. *J. Electrochem. Soc.* **2022**, *169* (9), No. 090507.

(54) Tang, J.; Luo, Q.; Wu, Z.; Shi, K. Single-crystalline Al-doped LiMn2O4 nanotubes for electrochemical lithium extraction from brines. *Chem. Eng. J.* **2025**, *505*, No. 159256.

(55) Tang, J.; Luo, Q.; Shi, K. Fabrication of single-crystal Li-rich manganese oxides as the electrode for electrochemical lithium extraction. *Ceram. Int.* **2025**, *51* (26), 51526−51534.

(56) Teychené, J.; Balmann, H. R.-d.; Maron, L.; Galier, S. Investigation of ions hydration using molecular modeling. *J. Mol. Liq.* **2019**, *294*, No. 111394.

(57) Trocoli, R.; Battistel, A.; Mantia, F. L. Selectivity of a lithium-recovery process based on LiFePO4. *Chemistry* **2014**, *20* (32), 9888−9891.